Twin nucleation and migration in FeCr single crystals

L. Patriarca[a], Wael Abuzaid[b], Huseyin Sehitoglu[b,*], Hans J. Maier[c], Y. Chumlyakov[d]

[a]Politecnico di Milano, Department of Mechanical Engineering, Via La Masa 34, I-20156 Milano, Italy
[b]Department of Mechanical Science and Engineering, University of Illinois at Urbana-Champaign, 1206 W. Green St., Urbana, IL 61801, USA
[c]Lehrstuhl für Werkstoffkunde (Materials Science), University of Paderborn, 33095 Paderborn, Germany
[d]Physics of Plasticity and Strength of Materials Laboratory, Siberian Physical and Technical Institute, 634050 Tomsk, Russia

ARTICLE DATA

ABSTRACT

Tension and compression experiments were conducted on body-centered cubic Fe -47.8 at pct. Cr single crystals. The critical resolved shear stress (CRSS) magnitudes for slip nucleation, twin nucleation and twin migration were established. We show that the nucleation of slip occurs at a CRSS of about 88 MPa, while twinning nucleates at a CRSS of about 191 MPa with an associated load drop. Following twin nucleation, twin migration proceeds at a CRSS that is lower than the initiation stress (≈114–153 MPa). The experimental results of the nucleation stresses indicate that the Schmid law holds to a first approximation for the slip and twin nucleation cases, but to a lesser extent for twin migration particularly when considerable slip strains preceded twinning. The CRSSs were determined experimentally using digital image correlation (DIC) in conjunction with electron back scattering diffraction (EBSD). The DIC measurements enabled pinpointing the precise stress on the stress–strain curves where twins or slip were activated. The crystal orientations were obtained using EBSD and used to determine the activated twin and slip systems through trace analysis.

1. Introduction

Understanding the deformation response of iron based body-centered cubic (bcc) alloys has significant merit, as these alloys form the basis of materials that are widely utilized in structures. Depending on the alloy composition and in particular grain orientations, twinning can occur in conjunction with slip resulting in complex mechanical behavior. In bcc materials a twin typically nucleates with an abrupt load drop, in some cases even in the 'elastic' region of the stress–strain curve [1,2]. Following twin nucleation at a critical resolved shear stress (CRSS) level τ^T, twin migration proceeds at a stress level τ^M that is lower. Twin migration is also the result of twin–twin and twin–slip dislocation reactions occurring at twin boundaries. Experimental evidence of twin migration, supported by local

strain measurements, can provide further insight for developments of bcc plasticity models, in particular on the hardening effect related to twin growth induced by twin/slip interactions. From the experimental point of view, measuring τ^T and τ^M requires local strain measurements and knowledge of the activated twin systems. In this study, we utilize local strain measurements from high resolution digital image correlation (DIC) to establish the twin nucleation and migration stresses. Accurate measurements of the CRSSs τ^T and τ^M allow us to provide valuable information for an initial evaluation of the Schmid law for bcc twinning, in particular for the migration stress. The Schmid law has been utilized for slip [3,4] and twinning [5] in face-centered cubic (fcc) crystals. For bcc slip, deviation from the Schmid law is well known [6–8]. Since the present study also allows measurements of the critical stress

---

* *Corresponding author.* Tel.: +1 217 333 4112; fax: +1 217 244 6534.
E-mail address: huseyin@illinois.edu (H. Sehitoglu).

for slip τ^s, we provide a critical check on the Schmid law for slip as well.

The majority of the previous investigations on FeCr have been undertaken on polycrystals [9–14]. In this study we utilize single crystals to activate specific twin and slip systems. This approach has been successfully employed in our previous work on fcc metals [15]. Based on the results of our experiments, we broadly classify four general types of single crystal deformation behaviors (Fig. 1).

For Case I, twinning represents the main deformation mechanism and it initiates within the elastic region of the stress–strain curve. Twin–twin interactions govern hardening behavior for this case. In Case II the hardening behavior is governed by twin–slip interactions and twin nucleation is preceded by pronounced slip activity. Case III represents orientations with a limited number of activated slip systems (1 or 2 slip systems). Finally, Case IV represents the occurrence of multiple-slip systems (>2 slip systems) with clear evidence of hardening. Examples of each one of the four cases will be given in the Results section along with the critical stress magnitudes and the activated twin/slip systems.

The Fe–Cr alloy is chosen as it shows twinning at room temperature. In earlier works on a Fe–47.8Cr alloy, Marcinkowski conducted indentation experiments and observed the presence of twinning and slip predominantly on <111>{112} systems [14].

Since it is not easy to identify the slip and twin systems coinciding with {112} planes by simple optical observations, we utilized DIC and Electron Back Scattering Diffraction (EBSD), as the combination of these tools facilitates this distinction. Indexing the twin systems with EBSD and measuring local strain fields allow us to monitor the nucleation and evolution of both slip and twinning during deformation. Particular emphasis is placed on the analysis of the deformation mechanism at the early stages of plasticity (either corresponding to first yielding or twin migration subsequent to the load drop). DIC was utilized at higher resolutions compared to conventional studies and provides microscale resolution measurements and allows pinpointing strain localizations due to slip and twin activation.

In summary, based on the four cases illustrated in Fig. 1, we address the following main issues: (i) the advancement of DIC methods using *ex situ* and stitching techniques to obtain local strain measurements which, in conjunction with EBSD, can be used to identify and determine the activated twin and slip systems; (ii) depending on the crystal orientation, the precise determination of the critical stress for twin (τ^T) and slip nucleation (τ^S), by pinpointing local strain disturbances using DIC. Therefore, we discuss the implications of these experimentally determined stresses with respect to the Schmid law; (iii) making a distinction between twin nucleation τ^T and twin migration τ^M critical stresses; (iv) the interactions of twins,
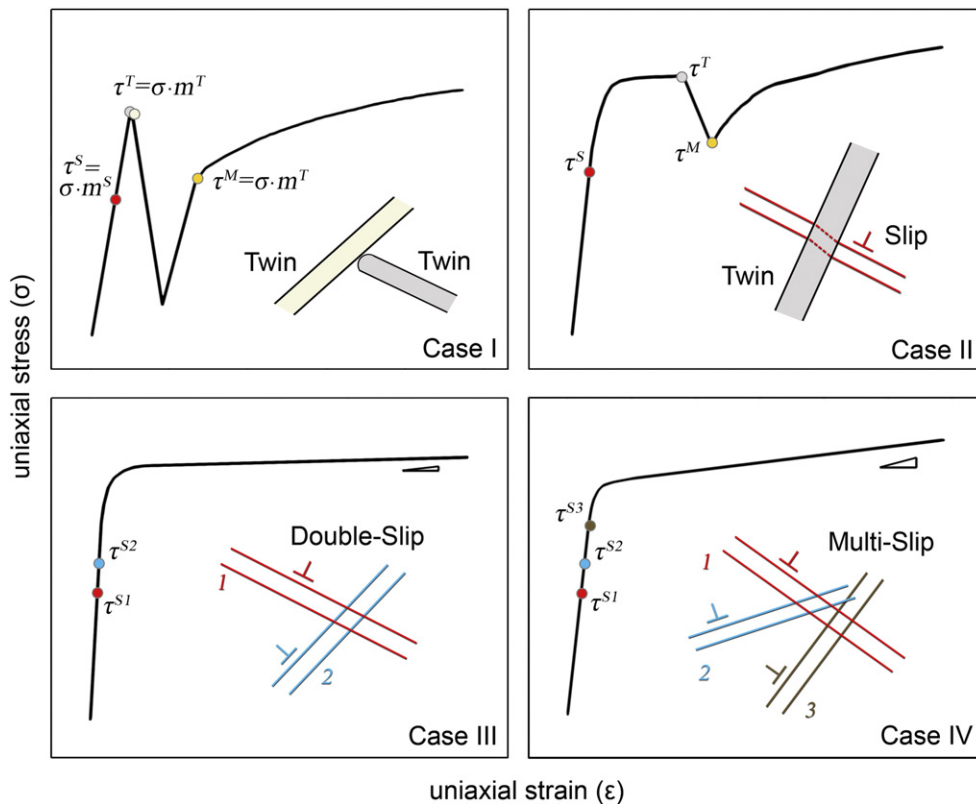

Fig. 1 – Schematic of the possible crystal deformation behaviors. The CRSSs for slip nucleation (τ^S), twin nucleation (τ^T) and twin migration (τ^M) are determined by multiplying the axial stress in the loading direction with the Schmid factors for the active slip (m^S) and/or twin (m^T) systems. Case I represents crystal hardening governed by twin–twin interactions. In Case II large slip activity precedes twin nucleation and twin–slip interactions dominate the hardening. Case III represents crystal orientations characterized by a limited number of activated slip systems. In Case IV multiple slip systems develop leading to crystal hardening.

in particular their influence on the formation of large local strains and increase in hardening; and (v) the cases of slip–twin interaction, which leads to impedance of slip and ensuing strain hardening as confirmed with DIC results. To address these issues, we conducted experiments on selected single crystals of bcc FeCr. The experimental details and the tested crystal orientations are given in Section 2. Section 3 provides theoretical analysis of the possible twin/slip systems based on Schmid factor analysis. The results are reported in Section 4 and discussed in Section 5.

2. Material and Methods

Single crystals of FeCr with a composition of 47.8 at.% Cr were manufactured using the Bridgman technique in a He atmosphere. Tensile dog-bone shaped specimens with a 1.5 mm×3 mm cross-section and a 10 mm gage length were electro-discharged machined (EDM) with the loading axis along the $[0\bar{1}0]$ and $[\bar{1}0\bar{1}]$ crystallographic directions. Compression samples were also sectioned into 4 mm x 4 mm x 10 mm using EDM. The loading axis was normal to the $[\bar{1}0\bar{1}]$, $[\bar{1}1\bar{1}]$, $[0\bar{1}0]$, and [314] planes and parallel to the 10 mm side of the sample. The crystallographic orientations in the other two directions, i.e., across the width and through the thickness of each sample, were determined using EBSD. Prior to loading, all samples were solution annealed at 900 °C for 1 h followed by a water quench. Table 1 lists all the samples tested in this study along with the crystal orientations, loading conditions and the number of repeated experiments.

The experiments were conducted at room temperature by means of a servo hydraulic load frame. Tension experiments were conducted in strain control, using a 5 mm gage length extensometer, while compression experiments were run in displacement control, both at a strain rate of 5×10^{-5} s^{-1}. Digital image correlation [16–19] was used to measure the evolution of local strains, in situ, on a full field basis. In addition to in situ DIC (sample under stress in the load frame), we also used higher resolution DIC strain measurements obtained ex situ (out of the load frame) for analyzing the local effect of slip and twinning. For in situ DIC, reference and deformed images were captured using an IMI model IMB-202 FT CCD camera (1600×1200 pixels) with a Navitar optical lens, the resolved resolution was 3.0 μm per pixel. The speckle pattern for DIC was obtained using black paint and an Iwata Micron B airbrush. Real time deformation measurements were made on a 3 mm×4 mm region using this setup. As deformation measurements are made real time, the onset of slip, twin nucleation and twin migration can be evaluated using the full field strain contour plots obtained.

For ex situ DIC, an optical microscope was used to capture the reference and deformed images. The microscope allows the images to be captured at a much higher magnification compared to the in situ images (2× versus 10× for ex situ). The increased imaging magnification improves the DIC measurement resolution (3.0 μm/pixel versus 0.44 μm/pixel for ex situ) [20] and enables better characterization of the local strain magnitudes that are associated with twin–twin, twin–slip and slip–slip interaction regions as will be shown in the Results section. Ex situ measurements were also used to define the onset of slip since, in some cases, strain localizations induced by slip required higher resolution DIC images.

3. Activated Slip and Twin Systems

The most commonly observed slip planes in bcc materials are the {112}, {011} and {123} types, while twinning is restricted to the {112} family. In both twinning and slip the shear directions are from the <111> family. The activation of certain twin/slip systems depends on both the crystal orientation and the loading direction (tension versus compression). One of the widely used approaches to establish the activated slip/twin systems is the calculation of the resolved shear stress on the slip/twin plane using Schmid factors [4]: m^S for slip and m^T for twinning. $m^{S/T}$ are defined as

$$\tau^{S/T} = \sigma \cdot m^{S/T} = \sigma \cdot \cos(\lambda)\cos(\varphi)$$

in which λ is the angle between the slip direction and the tensile axis, φ the angle between the tensile axis and the slip–plane normal. Based on the Schmid factor magnitude the stereographic triangles in Fig. 2 report the theoretical slip/twin systems for a bcc crystal structure. The distinction between tension and compression is necessary since bcc twinning, unlike slip, is uni-directional, i.e. there exists a unique sign of the shear stress direction (twinning direction) that leads to twinning [21,22]. The red line in each of the stereographic triangles separates the regions in which the crystal orientations are expected to display twinning in addition to slip from regions where only slip is predicted. This line is defined based on the magnitudes of the $m^{S/T}$ for the possible twin and slip systems. In our analysis, the <111>{112} twin systems having m^T larger than 0.35 or, alternatively, much higher than the m^S for <111>{112} slip is used as a criteria to define the regions (red line) where twinning is expected.

Table 2 lists all the crystal orientations used in this work along with the theoretically possible slip and twin systems. The Axis column refers to the orientation of the crystal in the load direction of the sample, henceforth referred to as orientation. We report the theoretical slip/twin systems (column: System) displaying the highest magnitudes of $m^{S/T}$. Using this table it is possible to predict the activated twin and slip systems for the crystal orientations classified in the experimentally observed Cases (schematic in Fig. 1). For Cases I and II, deformation via twinning is expected given the high m^T of the twin systems listed in Table 2. Crystal orientations belonging to Case III display a limited number of slip systems with high m^S ($[\bar{1}0\bar{1}]$ orientation in tension and [314] orientation

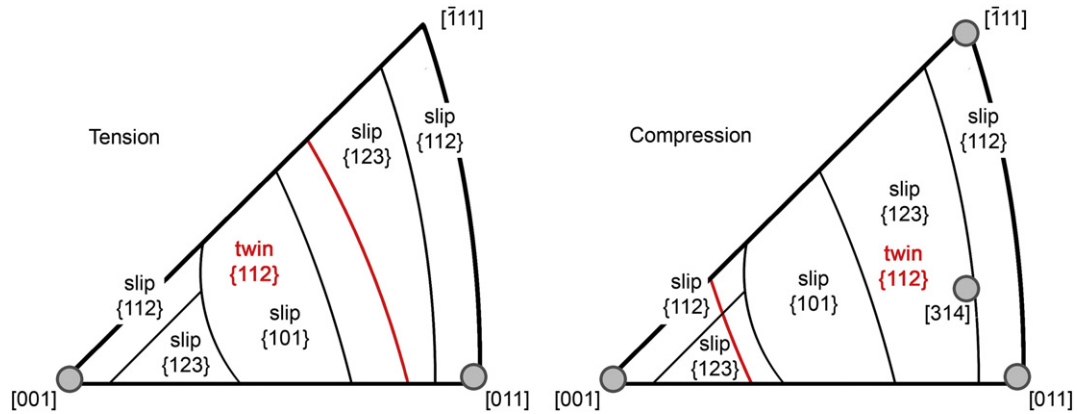| Table 1 – Crystal orientations and number of repeated experiments.						
	Tensile		Compressive			
Axis	$[\bar{1}0\bar{1}]$	$[0\bar{1}0]$	$[\bar{1}0\bar{1}]$	$[0\bar{1}0]$	$[\bar{1}1\bar{1}]$	[314]
No. of experiments	3	10	3	4	6	4

Fig. 2 – Stereographic triangles displaying slip and twin systems with the largest $m^{S/T}$. Regions containing twin favored orientations are plotted considering the stress sign dependence for bcc twinning. The gray-filled points represent the crystal orientations tested in the present study.

in compression). Finally, we classify the $[0\bar{1}0]$ orientation in compression in Case IV as there are multiple slip systems with high m^S.

4.   Results

The experimental results are presented in the next four main sections. In Section 4.1 we present the results for the $[0\bar{1}0]$ orientation loaded in tension (twinning dominated, Case I). The compression results for the $[\bar{1}11]$ and $[\bar{1}01]$ orientations are reported in Section 4.2 (twin and slip, Case II). In Sections 4.3 and 4.4 we present the results for the cases in which only deformation via slip is active: double slip for the $[\bar{1}0\bar{1}]$ orientation in tension (Case III, Section 4.3); multi-slip for the $[0\bar{1}0]$ orientation in compression (Case IV, Section 4.4).

4.1.   Case I — Twinning and Strain Hardening Behavior

Fig. 3 shows the stress–strain curve for the $[0\bar{1}0]$ crystal orientation tested in tension. The reported strains on the x-axis correspond to the DIC field averages, i.e. average axial strain (in the load direction) in the region covered by DIC. In the nominally elastic region of the stress–strain curve, high resolution DIC measurements indicate localized slip initiation. This can be clearly seen in the inset image marked A in Fig. 3 (notice the high localized strains). Using the original crystal orientation, we project all of the possible slip planes (and twin planes) onto the sample's surface. For the inset marked A, the strains localize in bands with a slope that matches the trace of the $[\bar{1}1\bar{1}](121)$ slip system with $m^S = 0.47$. The stress level at which these localized strains appear marks the onset of slip $\sigma^S_{[0\bar{1}0]_t} = 181$ MPa. With knowledge of the stress at the onset of slip and the activated slip system (from trace analysis), we calculate the resolved shear stress at the onset of slip $\tau^S_{[0\bar{1}0]_t} = 85$ MPa.

With continued loading, a stress level is reached where a pronounced and instantaneous load drop is observed ($\sigma^T_{[0\bar{1}0]_t} = 373$ MPa). This load drop is associated with twin nucleation. Full field strain measurements show high strain localizations in four bands (inset marked B in Fig. 3), using trace analysis the activated twin systems are identified. All the activated twin

Table 2 – Theoretical slip and twin systems for the crystal orientations analyzed in this work. For each crystal orientation are reported the slip/twin systems displaying the largest $m^{S/T}$.

1	2	3	4	5	6	7	8	9	10	11	12
$[1\bar{1}1]$ $(\bar{1}12)$	$[1\bar{1}1]$ $(1\bar{2}1)$	$[1\bar{1}1]$ (211)	$[\bar{1}11]$ $(1\bar{1}2)$	$[\bar{1}11]$ $(12\bar{1})$	$[\bar{1}11]$ $(\bar{2}11)$	$[111]$ $(1\bar{1}2)$	$[111]$ $(\bar{1}21)$	$[111]$ $(2\bar{1}1)$	$[\bar{1}\bar{1}1]$ (112)	$[\bar{1}\bar{1}1]$ $(12\bar{1})$	$[\bar{1}\bar{1}1]$ $(2\bar{1}\bar{1})$

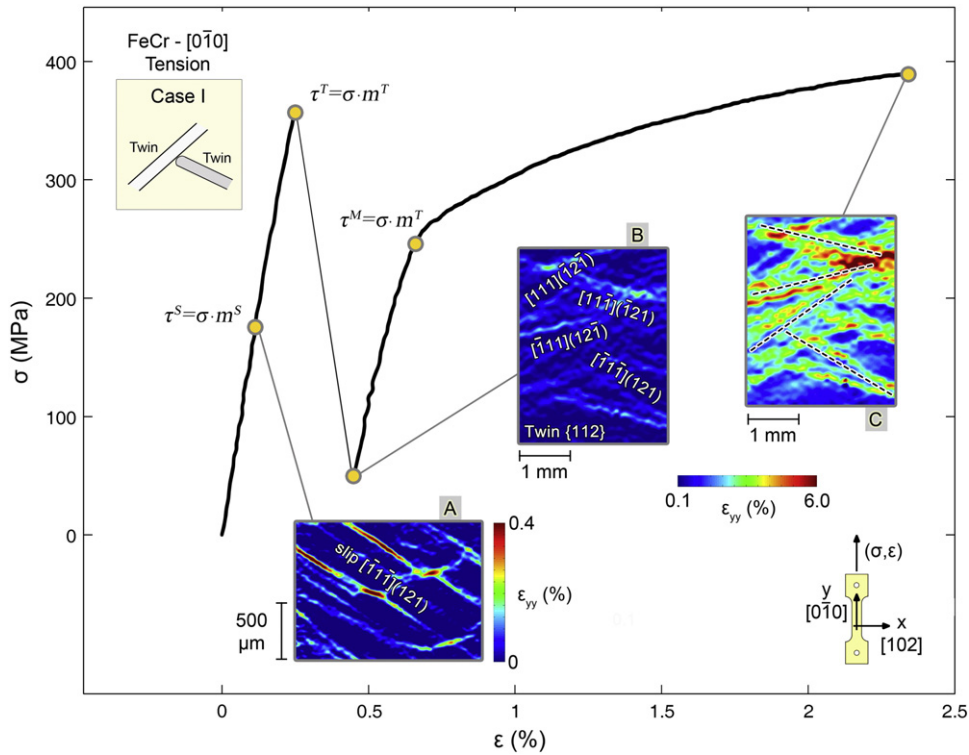|		Axis		Case		Slip			Twin		
						System	m^S		System	m^T	
Tensile		$[\bar{1}0\bar{1}]$		III		2, 8	0.47		1, 3, 7, 9	0.24	
		$[0\bar{1}0]$		I		2, 5, 8, 11	0.47		2, 5, 8, 11	0.47	
Compressive		$[\bar{1}0\bar{1}]$		II		2, 8	0.47		2, 8	0.47	
							0.47				
		$[0\bar{1}0]$		IV		2, 5, 8, 11	0.47		1, 3, 4, 6, 7, 9, 10, 12	0.24	
		$[\bar{1}11]$		II		4, 8, 12	0.31		4, 8, 12	0.31	
		$[314]$		III		2	0.49		2	0.49	
						$[1\bar{1}1](\bar{1}3\bar{2})$	0.50				

Fig. 3 – Stress–strain curve and DIC strain measurements for $[0\bar{1}0]$ orientation in tension (Case I). The inset image marked A shows localized strains due to onset of slip. Proceeding along the stress–strain curve the load drop indicates twin nucleation at τ^T. The inset image marked B displays localization of strains due to the nucleation of four twin systems in the <111>{112} family. Twin migration starts at τ^M and produces the local strain increments visualized in the inset image marked C in the same regions (bands) formed at τ^T.

systems have the same $m^T=0.47$, and the critical resolved shear stress for twin nucleation is obtained as $\tau^T_{[0\bar{1}0]t} = 177\,MPa$. Following the load drop associated with twin nucleation, the material appears to deform elastically as shown by the second linear region of the stress–strain curve in Fig. 3. With additional loading, plastic response is observed at a stress that is *lower* than the stress reached prior to twin nucleation. The strain accumulation beyond this point takes place in the same regions (bands) that were linked to twin nucleation (inset market C, Fig. 3). The strain level increases as well as the width of the bands. These observations indicate that the plastic response may be dominated by twin migration. Consequently, we mark the onset of twin migration $\tau^M_{[0\bar{1}0]t} = 114\,MPa$ (Fig. 3) the stress level at which plastic strains start to accumulate in the same bands that formed following twin nucleation.

The determination of the activated twin and slip systems using high resolution DIC was confirmed through EBSD measurements and SEM images. Fig. 4 reports post-experiment EBSD data of the local crystal orientation for a 400 μm × 200 μm region on the sample's surface. The red-colored field represents the orientation of the matrix (very close to the original crystal orientation). Blue and green points indicate regions displaying a different crystal orientation. For both regions, the misorientation with the matrix is about 60°, this indicates that the regions are twinned. The slope on the observed twins matches with the traces of $[11\bar{1}](\bar{1}21)$ and $[\bar{1}11](12\bar{1})$ twin systems. The same two

twins are also obvious from the SEM image in Fig. 4. In addition, the trace of the $[\bar{1}1\bar{1}](121)$ slip system can be detected in the upper right corner of the SEM image. Both of these observations are in good agreement with the results obtained from the *ex situ* strain field and trace analysis previously reported in the inset images A and B in Fig. 3.

Further experiments using *ex situ* DIC (high magnification images obtained using the optical microscope) provide higher resolution strain measurements compared to what is possible *in situ*. With improved resolution, the strains associated with twin–twin interaction can be characterized as shown in Fig. 5. The two crossing twins shown in the figure lead to high strains in the interaction region $\varepsilon^{T-T}_{yy,res} \approx 10\%$, while relatively low strains are measured in the surrounding matrix. This can be clearly seen by comparing the magnitude of strain localization due to twin–twin intersection, $\varepsilon^{T-T}_{yy,res} \approx 10\%$, with the nominal mean value of the residual strain in the specimen, $\varepsilon^{mean}_{yy,res}=0.32\%$.

4.2.   Case II — Twin–Slip Interaction

Fig. 6 displays the stress–strain curve for a $[\bar{1}1\bar{1}]$ oriented sample loaded in compression (Case II). High resolution DIC measurements (inset image marked A) reveal slip on the $[111](1\bar{2}1)$ system with $m^S=0.31$ at $\sigma^S_{[\bar{1}1\bar{1}]c} = 284\,MPa$, leading to a CRRS of $\tau^S_{[\bar{1}1\bar{1}]c} = 88\,MPa$. Slip on the same system accumulates up to $\varepsilon_B=1.07\%$ (inset image marked B). No traces of slip on other systems are observed. With activation of only a
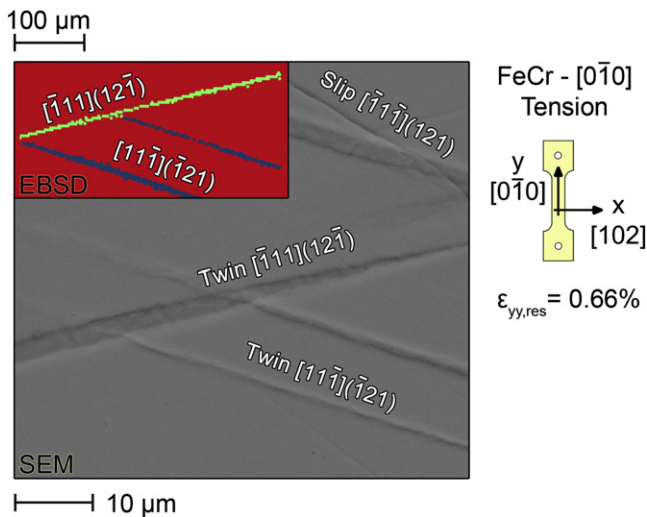
Fig. 4 – EBSD data and SEM image for $[0\bar{1}0]$ orientation in tension (Case I). The EBSD data represent a 400 μm × 200 μm region on the sample's surface. Red-colored points indicate the crystal orientation of the matrix. Green and blue points indicate, respectively, $[\bar{1}11](12\bar{1})$ and $[11\bar{1}](\bar{1}21)$ twin systems as these two regions show a misorientation (with respect to the matrix crystal orientation) of about 60°. The SEM image also displays a trace of the $[\bar{1}1\bar{1}](121)$ slip system.

single slip system, no significant hardening resulted as seen by the low slope of the stress–strain curve ($h = d\sigma/d\varepsilon = 0.003E$). Proceeding with loading, we observe twinning nucleating with a stress drop. Three twin systems were activated at a critical stress $\sigma^T_{[\bar{1}11]_c} = 646$ MPa leading to a CRRS for twin nucleation of $\tau^T_{[\bar{1}11]_c} = 203$ MPa. The inset image marked C displays the strain field after twin nucleation of the three observed twin systems $[111](1\bar{2}1)$, $[1\bar{1}\bar{1}](1\bar{1}2)$ and $[\bar{1}1\bar{1}](2\bar{1}1)$.

For improved characterization of the strains in the interaction regions, we again utilized high resolution *ex situ* DIC. Fig. 7
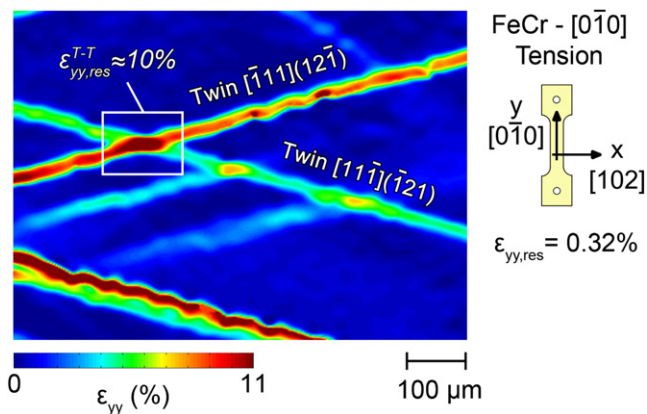

Fig. 5 – High-resolution DIC contour plot for the $[0\bar{1}0]$ orientation in tension (Case I). The intersection line between twin planes $(12\bar{1})$ and $(\bar{1}21)$ is parallel to the $[\bar{1}0\bar{1}]$ direction.

shows a residual strain field obtained with high resolution DIC for the $[\bar{1}1\bar{1}]$ orientation in compression. Strain fields display the effect of the mutual interaction between $[1\bar{1}\bar{1}](1\bar{1}2)$ and $[111](1\bar{2}1)$ twin systems and the $[\bar{1}1\bar{1}](2\bar{1}1)$ slip system. Twin–slip intersection regions exhibit high localized strains ($\varepsilon^{T-S}_{yy,res} \approx 6\%$, $\varepsilon^{mean}_{yy,res} = 2.4\%$, Fig. 7). The twin–twin intersection is shown to provide higher localized strains ($\varepsilon^{T-T}_{yy,res} \approx 8\%$, Fig. 7) than the twin–slip case. The results presented in Figs. 6 and 7 for the $[\bar{1}1\bar{1}]$ orientation show evidence of high local strains for both twin and slip. It follows that accurate assessment of strain accumulation induced by twin migration for that sample is not possible. To address this issue, we analyze a similar case of crystal orientation leading to twin–slip interaction on a $[\bar{1}0\bar{1}]$ sample, having the same mechanical behavior as the $[\bar{1}1\bar{1}]$ orientation (both $[\bar{1}1\bar{1}]$ and $[\bar{1}0\bar{1}]$ orientations are classified as Case II).

The stress–strain curve for the $[\bar{1}0\bar{1}]$ orientation is shown in Fig. 8. In the DIC analysis, particular emphasis is on twin migration. Three critical *in situ* strain fields are analyzed. The inset image marked A indicates activation of the $[111](1\bar{2}1)$ slip system with $m^S = 0.47$ occurring at $\sigma^S_{[\bar{1}0\bar{1}]_c} = 185$ MPa leading to a CRRS of $\tau^S_{[\bar{1}0\bar{1}]_c} = 87$ MPa. Proceeding along the stress–strain curve, at point B ($\sigma^T_{[\bar{1}0\bar{1}]_c} = 413$ MPa) the occurrence of the load drop indicates twin nucleation. Trace analysis indicates twin nucleation on $[1\bar{1}1](121)$ and $[111](1\bar{2}1)$ systems ($\tau^T_{[\bar{1}0\bar{1}]_c} = 194$ MPa). Incremental DIC is used to analyze the evolution of the axial strain field between point C (following twin nucleation) and C^i, the correlation is implemented using the image at point C as the reference. The strains displayed in the inset image marked C–C^i represent strain accumulation between C and C^1 only. Referring to this inset image two observations are provided. (i) Twins nucleated in a region different from the preceding region displaying slip (inset image marked B). (ii) The strain accumulation between point C and C^i takes place in the same regions (bands) that were linked to twin nucleation. These observations indicate that the plastic response may be dominated by twin migration. The stress level at which plastic strains start to accumulate in the same bands that formed following twin nucleation marks the onset of twin migration $\tau^M_{[\bar{1}0\bar{1}]_c} = 149$ MPa. Beyond point C^i, another load drop is observed, this indicates the nucleation of additional twins.

4.3. Case III — Double Slip

Case III represents cases characterized by limited number of activated slip systems (Table 2). Fig. 9 shows the stress–strain curve of a $[\bar{1}0\bar{1}]$ oriented sample in tension. For the inset marked A, the strains localize in bands with a slope that matches the trace of the $[111](1\bar{2}1)$ slip system ($m^S = 0.47$), leading to a CRSS of $\tau^S_{[\bar{1}0\bar{1}]} = 87$ MPa. By following the evolution of the axial strain fields through the *in situ* DIC measurements (inset images marked A, B, C and D) we observe higher strains developing still on bands corresponding to the $[111](1\bar{2}1)$ slip system. Traces of slip on the $[1\bar{1}1](121)$ system are also detected (inset images marked B, C and D).

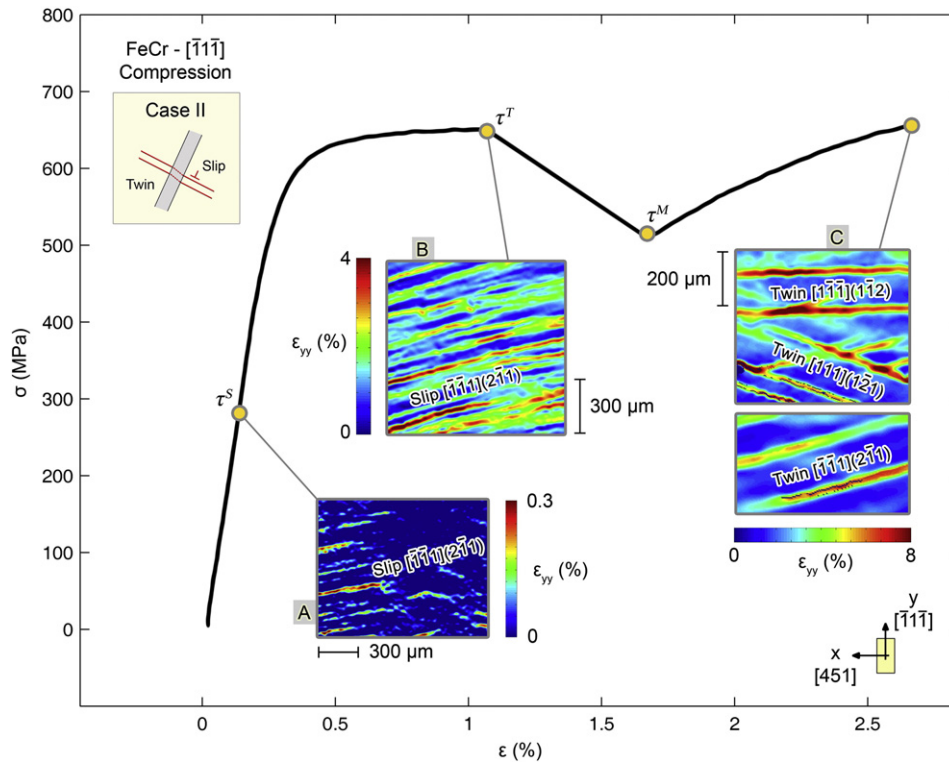**Fig. 6 – Stress–strain curve and DIC strain field measurements for $[\bar{1}1\bar{1}]$ orientation in compression (Case II). Inset image marked A shows traces of localized slip on the $[\bar{1}1\bar{1}](2\bar{1}1)$ system. Slip develops on the same systems until the onset of twin nucleation (inset image marked B). The inset image marked C displays the strain localizations introduced by the nucleation of three twin systems from the <111>{112} family. All the strain plots are obtained using *ex situ* high resolution DIC.**

The *in situ* DIC also shows that the activated slip systems accommodate deformation differently. To elucidate the difference, we utilize high resolution *ex situ* axial strain measurements.
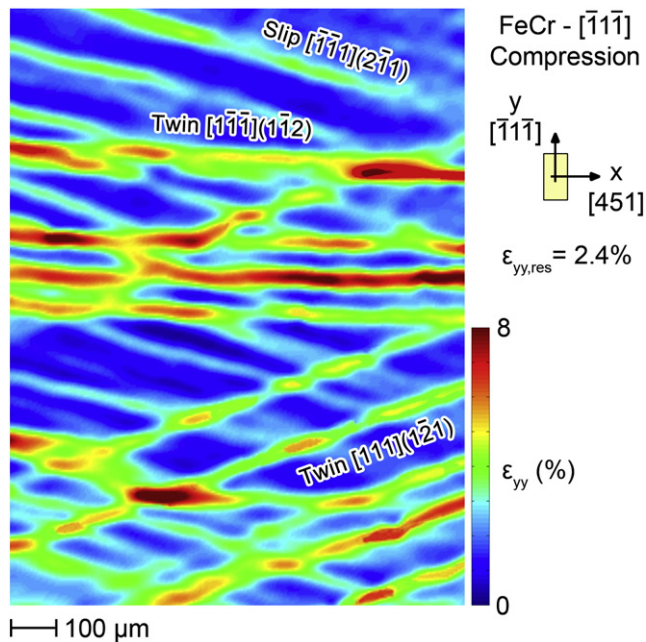

Fig. 7 – Local strain measurements using high-resolution DIC on a $[\bar{1}1\bar{1}]$ oriented sample in compression (Case II).

Fig. 10 reveals again how the slip system $[111](1\bar{2}1)$ provides higher strains at this stage of the deformation ($\varepsilon_{yy,res}=1.8\%$). This can be clearly seen from the inset image marked A where localized strains along the bands corresponding to the $[111](1\bar{2}1)$ slip system display axial strains up to 3%. The specific case of crystal orientation $[\bar{1}0\bar{1}]$ in tension is an example of the double slip case (Table 2). We draw the conclusion that for relatively low applied strains (up to $\varepsilon=3\%$) no hardening is observed since only one or two slip systems are active (Case III, double slip).

4.4.   Case IV — Multi-Slip

We classify the $[0\bar{1}0]$ orientation in compression as a multi-slip case (schematic in Fig. 1) since there are four possible slip systems in the <111>{112} family with high $m^S=0.47$ (Table 2). The stress–strain curve for this crystal orientation displays a constant hardening (Fig. 11). The inset image marked A represents the first evidence of strain localizations due to the activation of the $[111](\bar{1}2\bar{1})$ slip system at a CRRS of $\tau^S_{[0\bar{1}0]c} = 85$ MPa. Successively (inset image marked B), localized strain bands of the second slip system $[\bar{1}1\bar{1}](231)$ with $m^S = 0.46$ appear. The *in situ* axial strain plot (inset image marked C, Fig. 11) shows a direct evidence of the interaction between the two main slip systems involved in the crystal deformation. Moreover, the strain field displays strain bands oriented differently from the two main systems indicating the presence of other secondary slip systems involved, but not clearly
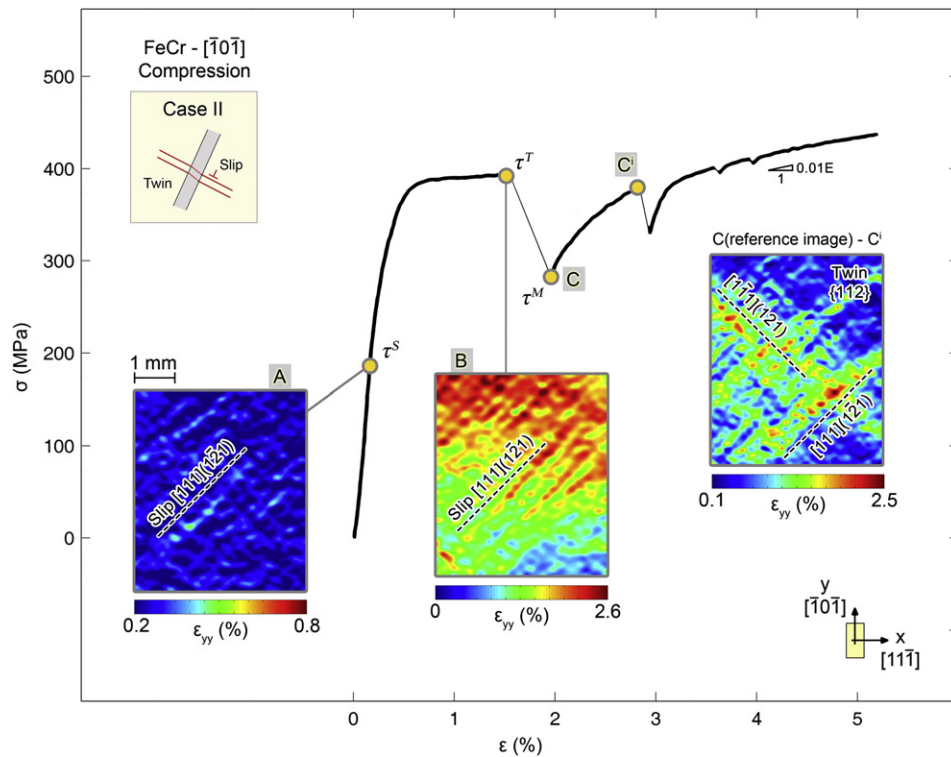
Fig. 8 – Stress–strain curve and DIC strain field measurements for $[\bar{1}0\bar{1}]$ orientation in compression (Case II). The inset image marked A shows the onset of localized slip on the $[111](1\bar{2}1)$ system. Slip on the same system proceeds until twin nucleation (inset image marked B). Incremental DIC is used to illustrate twin migration in the inset image marked C–C^i (see text for details).

visualized with the available DIC resolution. In this specific case, the slip systems involved lead to crystal hardening.

5.　Further Analysis of Results

Digital image correlation strain measurements were used to detect the localization of plastic strains associated with slip nucleation, twin nucleation, and twin migration in bcc single crystals. These local deformation measurements allow for the precise determination of the critical stresses associated with the activation of slip τ^S, twin τ^T, and twin migration τ^M which are otherwise not accessible utilizing nominal sample response measurements. For example, slip can occur locally despite the overall elastic response in a number of cases. Twin nucleation is associated with a sudden load drop and can be measured by various experimental techniques, but the subsequent migration can occur immediately after the load drop or after further deformation. *In situ* local strain measurements via DIC permitted measurement of the corresponding stress level at which twin migration initiates. The results from all the crystal orientations tested are summarized in Table 3. Further analysis and discussion of the main results is provided in this section.

　We classify the crystal orientations analyzed in four different cases (see schematic in Fig. 1). These four cases represent the possible crystal deformation behaviors based on the type of deformation mechanism involved (slip/twin). Each

case displays a crystal hardening that depends on of the main mechanism involved (twin–twin, twin/slip or slip/slip interactions). The real-time acquisition of the strain fields using DIC allowed capturing interesting features regarding the nucleation and interaction of slip and twinning. In particular, using DIC in conjunction with crystal orientations from EBSD, we simultaneously determined the systems (planes and directions) and the CRSSs for slip onset τ^S, twin nucleation τ^T and migration τ^M for each of the crystal orientation analyzed (Table 3). While for slip and twin nucleation we observe constant CRSSs, twin migration stresses display variations which we discuss in the following.

5.1.　Twin Migration Stress

In the experimental results reported in this paper, the twin migration stress σ^M (τ^M) represents the point of macroscopic yielding on the stress–strain curves subsequent to twin nucleation. In fact, as evident from DIC strain measurements (Figs. 3 and 8), strains localize starting from τ^M in the same region formed after the load drop. In Table 3, the reported values for the CRSS for twin migration show variation depending on crystal orientation. The CRSS magnitudes for the $[0\bar{1}0]$ orientation in tension was 114 MPa while for $[\bar{1}1\bar{1}]$ and $[\bar{1}0\bar{1}]$ orientations in compression about 153 MPa was measured. We classified the first case as Case I, and the second one as Case II.

　Two possible explanations are introduced to explain the difference in the CRSS values for twin migration for Cases I
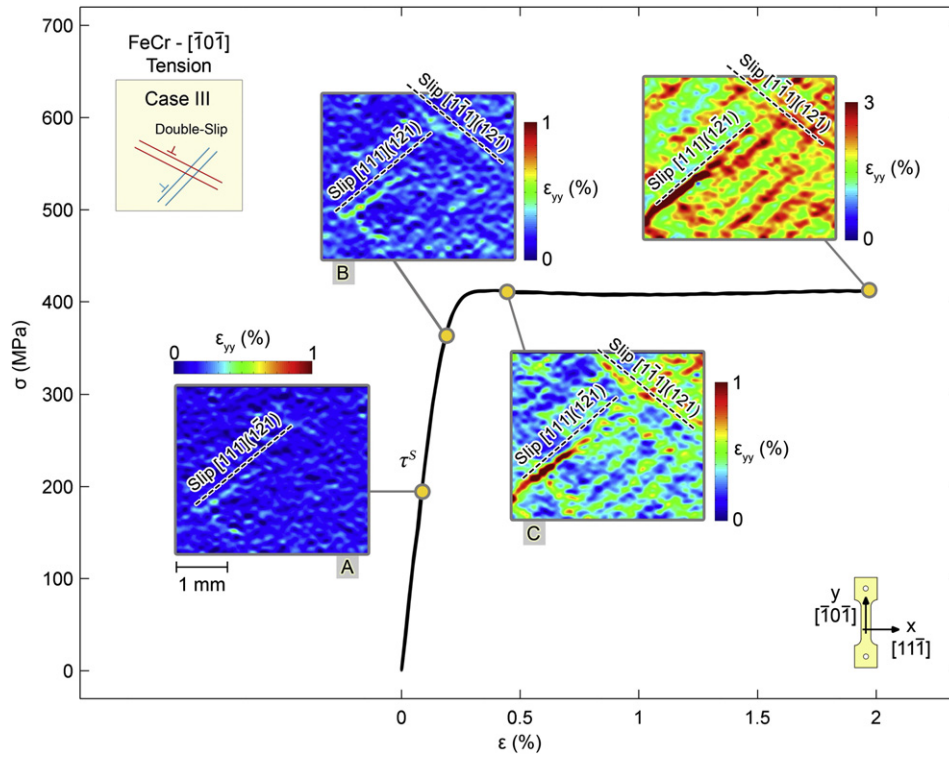
Fig. 9 – Stress–strain curve and DIC strain field measurement for the $[\bar{1}0\bar{1}]$ orientation in tension (Case III). The inset image marked A shows onset of slip on the $[111](1\bar{2}1)$ system. Slip on the same system proceeds with loading as shown in the inset images marked B–C–D. From the latter strain plots traces of slip on $[1\bar{1}1](121)$ system are also detected.
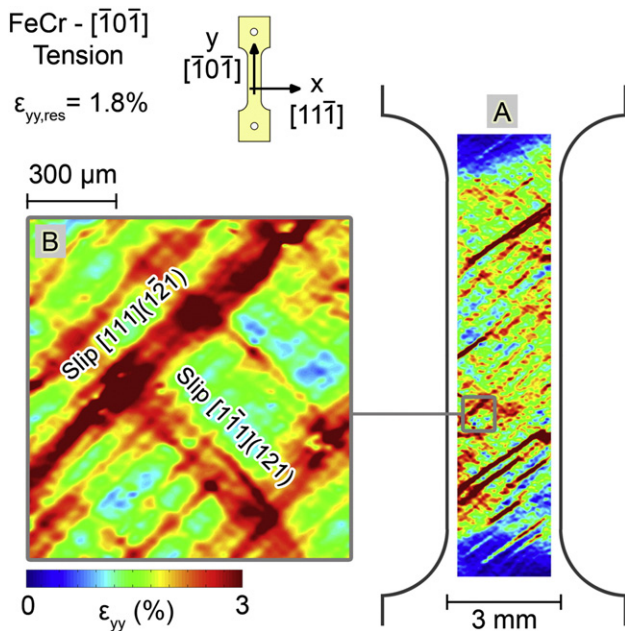

Fig. 10 – Local strain measurements using high-resolution DIC for the $[\bar{1}0\bar{1}]$ orientation in tension (Case III). The inset image marked A shows the residual strain field on the entire sample (low resolution DIC). The inset image marked B displays strain localizations along two traces corresponding to $[111](1\bar{2}1)$ and $[1\bar{1}1](121)$ slip systems (high resolution DIC).

and II. First of all, for the $[\bar{1}1\bar{1}]$ and $[\bar{1}0\bar{1}]$ crystal orientations in compression (Case II) twin nucleation is preceded by appreciable deformation (1.5% slip strain) developing in one primary slip system (Figs. 6 and 8). It is conceivable to argue that this large slip activity preceding twin nucleation influences the subsequent twin growth process. A growing twin can encounter slip bands [1] thus having difficulties in penetrating them. Secondly, twin growth is influenced by the dominant intersection mechanism involved, *i.e.* twin–twin (Case I) or twin–slip (Case II), hence the product of the dislocation reactions occurring in the intersection region. The high stresses in the intersecting regions can promote the dislocation reactions that facilitate twin growth. Therefore for Case I, where twin activity is not preceded by prior large slip activity, and twin–twin interaction (high local stress) is the primary intersection mechanism, we measured lower τ^M.

5.2. Strain Hardening

It is also well-known that twin–twin, twin–slip and slip–slip intersections have an important effect on the crystal hardening. As shown in a related work on fcc steel by Efstathiou et al. [15], the visualized accumulation of plastic deformation in the twin–twin and twin–slip intersection regions can be correlated with the observed crystal hardening. In our experiments, at the point where twin migration is observed (at twin migration stress σ^M (τ^M)) on the stress–strain curves, all the crystal orientations displaying twinning (leading to twin–twin and twin–slip interactions) show high values of the hardening parameter $h_M = d\sigma^M/d\varepsilon_{pl} = 0.2E$, and high localized strains (up to
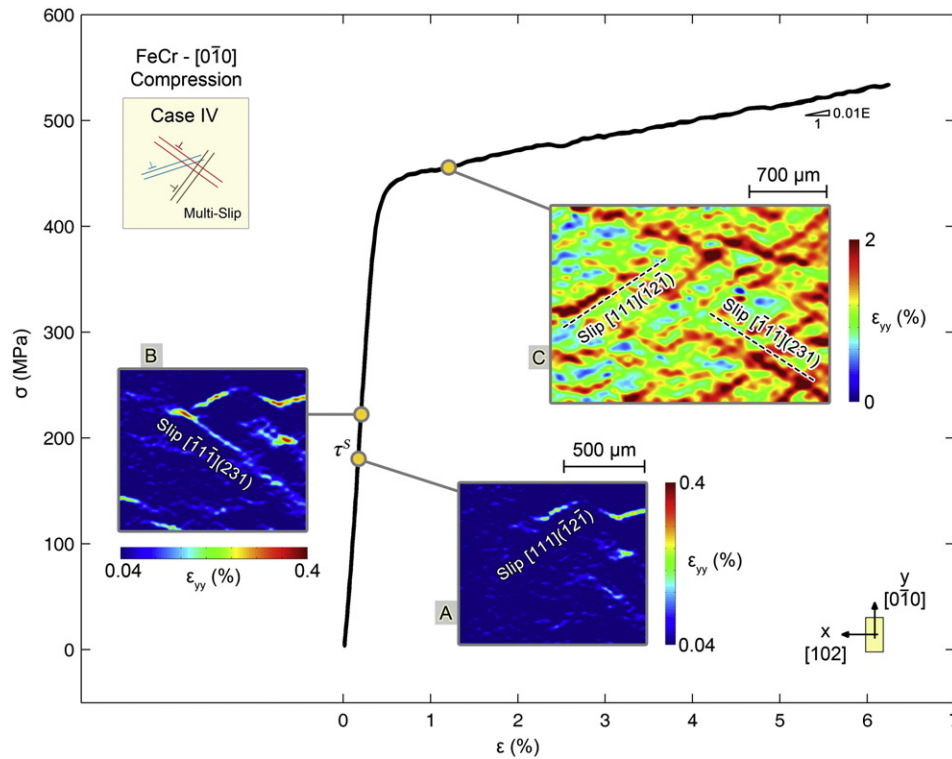
Fig. 11 – Stress–strain curve and DIC strain field measurement for the $[0\bar{1}0]$ orientation in compression (Case IV). The inset images marked A–B illustrate, respectively, slip onset on the $[111](\bar{1}2\bar{1})$ and $[\bar{1}1\bar{1}](231)$ systems. The inset image marked C displays evolution of the strain field and slip-slip interactions.

10% for the $[0\bar{1}0]$ orientation in tension, and up to 8% for the $[\bar{1}1\bar{1}]$ orientation in compression). For the same level of deformation, the double-slip case shows virtually no hardening ($[\bar{1}0\bar{1}]$ in tension, Case III, Fig. 9), while the multi-slip case analyzed ($[0\bar{1}0]$ in compression, Case IV, Fig. 11) displays a constant hardening modulus from the onset of macroscopic plasticity ($h=0.01E$) that is lower compared to the twin-twin and twin-slip cases. For both the cases displaying slip, the localized strains (up to 3%) are much lower than the localized strains measured for Cases I and II indicating that the level of strain accumulation in the region of twin/twin, twin/slip and slip/slip intersection can be correlated with the observed level of hardening.

5.3. Twin Nucleation Stress

For each of the crystal orientations displaying twinning ($[0\bar{1}0]$ in tension, $[\bar{1}1\bar{1}]$ and $[\bar{1}0\bar{1}]$ in compression, Table 2), a CRSS of about 191 MPa was measured for twin nucleation (see Table 3). Moreover, all the twin systems having the highest magnitudes of the Schmid factors m^T activate simultaneously. These observations support the prediction of the activated twin systems using Schmid factor analysis along with the knowledge of the twinning direction for each crystal orientation and load direction (see Section 3). The existence of a constant CRSS is noteworthy because if the measurement techniques are not precise, it is possible to report a deviation contrary to the current findings. For the crystal orientations $[0\bar{1}0]$ and [314] in compression, and $[\bar{1}0\bar{1}]$ in tension only slip is observed since the resolved shear stress for twinning is rather low $m^T=0.24$ (Table 2). The choice of single crystals in this study is rather unique to isolate specific mechanisms.

5.4. Slip Nucleation Stress

For all the crystal orientations tested in our study (Table 2), slip develops on planes and directions having the highest SFs, <111>{112} in most cases and <111>{123} in others. Using high resolution DIC measurements (3.0–0.44 μm/pixel) we pinpoint strain localization due to the slip onset appearing for each crystal orientation and load direction at a constant CRSS of 88 MPa. This type of resolution during deformation is rather unique. The results conform to the Schmid law for slip (Table 3)

Table 3 – CRRSs for onset of slip τ^S, twin nucleation τ^T, and twin migration τ^M as functions of the crystal orientation and load direction. The sequences S–T, and S–S refer to slip–twin and slip–slip cases.

Mechanism				Twinning (T)		Slip (S)
	Axis	Case	Sequence	τ^T (MPa)	τ^M (MPa)	τ^S (MPa)
Compressive	$[\bar{1}0\bar{1}]$	II	S–T	194±8	149±19	87±16
	$[0\bar{1}0]$	IV	S–S	Not observed		85
	$[\bar{1}1\bar{1}]$	II	S–T	203±3	157±3	88
	[314]	III	S–S	Not observed		91
Tensile	$[\bar{1}0\bar{1}]$	III	S–S	Not observed		93±1
	$[0\bar{1}0]$	I	S–T	177±13	114±3	85

and that slip precedes twin nucleation. Precise measurements are needed because slip nucleation in the elastic region of the stress–strain curve (see inset image marked A in Fig. 3, image resolution used for DIC is 0.9 µm/pixel) was detected which cannot be gleaned clearly from macroscopic observations.

Overall, the experimental results point to the utility of DIC to analyze the response of metals undergoing complex slip–twin evolution. The progression of these mechanisms are not readily explainable by macroscopic stress–strain measurements alone, and localized strain measurements shed light into the activation of slip and twinning during deformation and their interactions. Hence, the present approach provides insight for bridging the scales ranging from macroscopic response to localized behavior at microscales. The conclusions from this work are summarized in the next section.

6.   Conclusions

In this work, we experimentally studied the nucleation and evolution of slip and twinning in single crystals of bcc Fe–47.8Cr. Using high resolution strain field measurements we establish the CRSSs for slip/twin nucleation and twin migration. These results provide the basis for discussion of pertinent issues regarding deformation in bcc materials when both slip and twinning occur, and support the following conclusions:

(1) We classify the observed stress–strain behaviors in four different Cases (schematic in Fig. 1) based on the activated mechanisms (twin/slip) that lead to a different crystal hardening (twin-twin and twin–slip interactions display higher hardening than slip–slip interactions).

(2) For Case I (twinning dominated) we observe a lower CRSS for twin migration (114 MPa) compared to the Case II (153 MPa) where twin nucleation is preceded by significant slip activity.

(3) Twin nucleation occurs at an average CRSS of 191 MPa. For the cases analyzed in this study this observation suggests that a critical shear stress for twin nucleation holds to a first approximation.

(4) We establish that the nucleation of slip occurs at an average CRSS of 88 MPa and always precedes twin nucleation.

(5) We provide local strain measurements on twin–twin and twin–slip intersection regions for two specific crystal orientations. Twin–twin intersections lead to higher strain localizations (up to 10%) compared to the twin–slip case (up to 6%).

Acknowledgments

REFERENCES

[1] Christian JW, Mahajan S. Deformation twinning. Prog Mater Sci 1995;39:1.

[2] Reed-Hill RE, Hirth JP, Rogers HC, editors. Deformation twinning. New York–London–Paris, Gainesville, Florida: Gordon and Breach Science Publishers; 1963.

[3] Nabarro FRN. Extended dislocations and the Schmid law of resolved shear stress. Philos Mag 1966;14:861.

[4] Schmid E. Proc. Internat. Cong. Appl. Mech; 1924.

[5] Karaman I, Sehitoglu H, Beaudoin AJ, Chumlyakov YI, Maier HJ, Tomé CN. Modeling the deformation behavior of Hadfield steel single and polycrystals due to twinning and slip. Acta Mater 2000;48:2031.

[6] Vitek V, Mrovec M, Bassani JL. Influence of non-glide stresses on plastic flow: from atomistic to continuum modeling. Mater Sci Eng A 2004;365:31.

[7] Duesbery MS, Vitek V. Plastic anisotropy in b.c.c. transition metals. Acta Mater 1998;46:1481.

[8] Christian J. Some surprising features of the plastic deformation of body-centered cubic metals and alloys. Metall Mater Trans A 1983;14:1237.

[9] Kako K, Takaki S, Abiko K. Effect of grain size on the deformation properties of a high-purity Fe–50Cr alloy at 293 and 773 K. Sendai, JAPON: Japan Institute of Metals; 2000.

[10] Isozaki S, Takaki S, Abiko K. High temperature deformation mechanism of a high-purity Fe–50 mass% Cr alloy. Phys Status Solidi A 1998;167:471.

[11] Kako K, Isozaki S, Takaki S, Abiko K. Deformation mechanisms in high-purity Fe–50Cr(–5W) alloys at elevated temperatures. Phys Status Solidi A 1998;167:481.

[12] Mahajan S, Jin S, Brasen D. Micro-twinning in a spinodally decomposed Fe–Cr–Co alloy. Acta Metall 1980;28:971.

[13] Lagneborg R. Deformation in an iron-30% chromium alloy aged at 475 °C. Acta Metall 1967;15:1737.

[14] Marcinkowski MJ, Fisher RM, Szirmae A. Effect of 500 °C aging on the deformation behavior of an iron–chromium alloy. Trans Am Inst Min Metall Pet Eng 1964;230:676-89.

[15] Efstathiou C, Sehitoglu H. Strain hardening and heterogeneous deformation during twinning in Hadfield steel. Acta Mater 2009;58:1479.

[16] Bruck H, McNeill S, Sutton M, Peters W. Digital image correlation using Newton–Raphson method of partial differential correction. Exp Mech 1989;29:261.

[17] Sutton MA, Mingqi C, Peters WH, Chao YJ, McNeill SR. Application of an optimized digital correlation method to planar deformation analysis. Image Vis Comput 1986;4:143.

[18] Chu T, Ranson W, Sutton M. Applications of digital-image-correlation techniques to experimental mechanics. Exp Mech 1985;25:232.

[19] Sutton MA, Wolters WJ, Peters WH, Ranson WF, McNeill SR. Determination of displacements using an improved digital correlation method. Image Vis Comput 1983;1:133.

[20] Carroll J, Abuzaid W, Lambros J, Sehitoglu H. An experimental methodology to relate local strain to microstructural texture. Rev Sci Instrum 2010;81.

[21] S.A.W. Twinning and the origin of cleavage nuclei in α-iron. Acta Metall 1962;10:803.

[22] Sleeswyk AW, Helle JN. Zigzag configurations of twins in α-iron. Acta Metall 1961;9:344.